

## Electronic Supplementary Information

# Activated Charcoal-Mediated Non-Contact Carbothermal Reduction of TiO<sub>2</sub> for Controlled Synthesis of Magnéli Phase Titanium Suboxides

S. Amanda Ekanayake<sup>a</sup>, Aaron Seeber<sup>b</sup>, Joseph Olorunyomi<sup>a</sup>, Haoxin Mai<sup>a</sup>, Sanje Mahasivam<sup>c</sup>,  
Daksh Shah<sup>a,d</sup>, Junlin Lu<sup>a</sup>, Xiaoming Wen<sup>a</sup>, Nishanthini Sampath<sup>e</sup>, Simon L. Schumann<sup>e,f</sup>, Nicholas  
Cox<sup>e</sup>, Dehong Chen<sup>a\*</sup> and Rachel A. Caruso<sup>a\*</sup>

<sup>a</sup>*Applied Chemistry and Environmental Science, School of Science, STEM College, RMIT University,  
Melbourne, Victoria 3000, Australia*

<sup>b</sup>*CSIRO Manufacturing, Clayton, Victoria 3168, Australia*

<sup>c</sup>*Ian Potter NanoBioSensing Facility, NanoBiotechnology Research Laboratory, School of Science,  
RMIT University, Melbourne, Victoria 3000, Australia*

<sup>d</sup>*CSIRO Energy, Clayton, Victoria 3168, Australia*

<sup>e</sup>*Research School of Chemistry, Australian National University, Acton, ACT 2601 Australia*

<sup>f</sup>*TU Dortmund University, Department of Chemistry and Chemical Biology, Otto Hahn-Strasse 6, 44227  
Dortmund, Germany*

\* Corresponding authors: [dhchen@qust.edu.cn](mailto:dhchen@qust.edu.cn) and [rachel.caruso@rmit.edu.au](mailto:rachel.caruso@rmit.edu.au)

## Solar steam generation experiments

Solar steam generation experiments were performed using a solar simulator (OAI Class AAA Solar simulator) with an AM 1.5 filter (1.0 sun irradiation,  $1000 \text{ W m}^{-2}$ ). In a typical experiment, an electronic balance (0.0001 g accuracy) was placed directly under the lamp of the solar simulator. To a 100 mL glass beaker, 80 mL of Milli-Q water was added and the beaker was placed on the electronic balance. The aerogel was then placed on the surface of water in the beaker, as shown in Figure S1. A portable thermocouple was used to measure the temperature on the surface of the aerogel. Prior to illumination, the aerogel was allowed to reach water absorption equilibrium for 30 min. After this, the lamp was turned on and weight loss of the water was monitored by measuring the weight of the beaker every 10 min for 1 h.

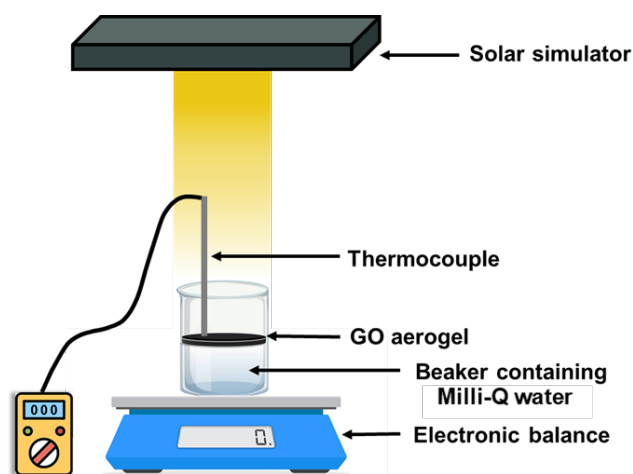


**Figure S1:** Schematic diagram of the apparatus used in solar steam generation experiments.

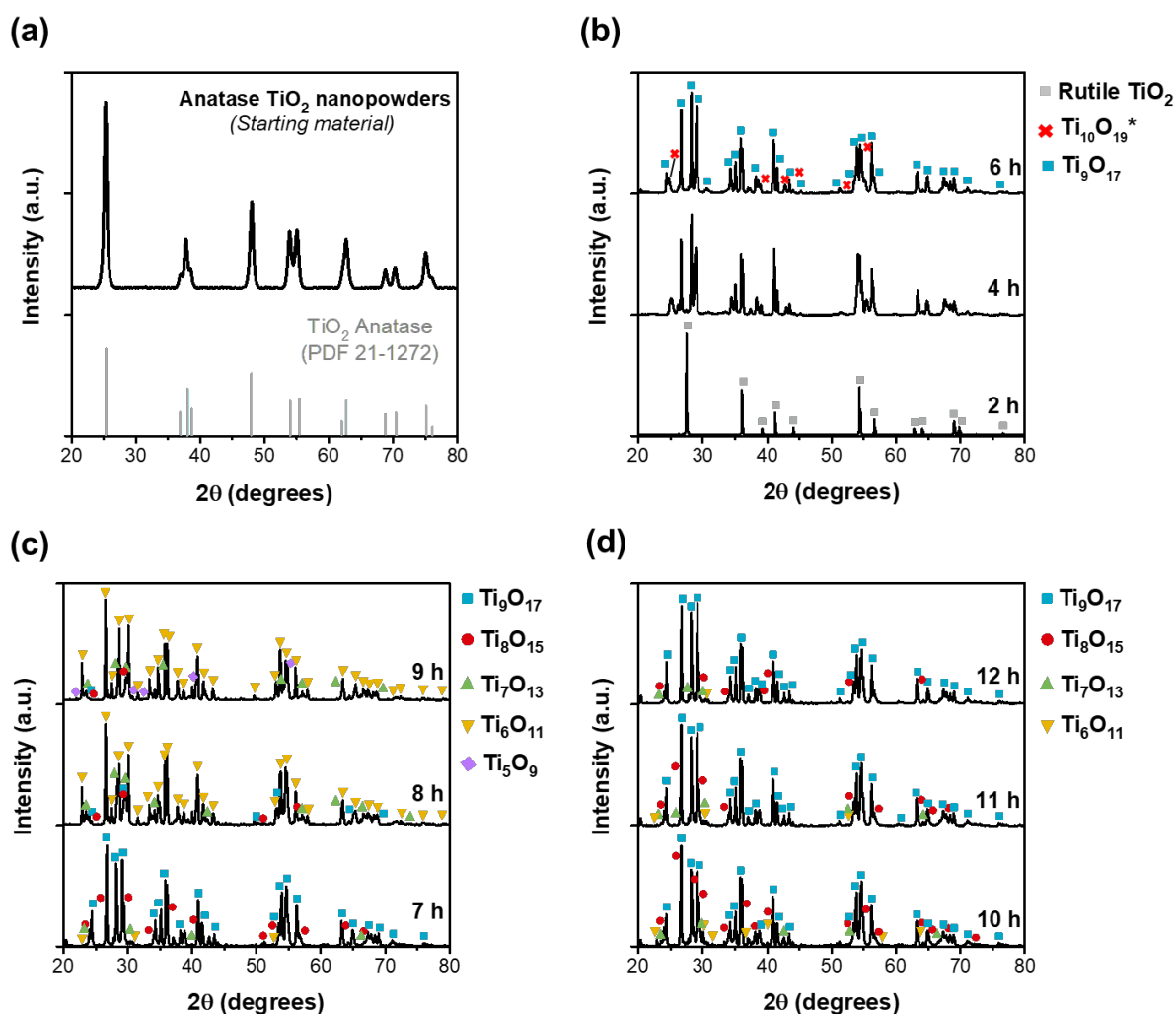


**Figure S2:** X-ray diffractograms of (a) anatase TiO<sub>2</sub> and (b-d) TiO<sub>2-x</sub> synthesised via carbothermal reduction at 1100 °C for different durations (as marked).

The diffractograms related to TiO<sub>2</sub> and obtained Magnéli phase titanium suboxides were matched with the following powder diffraction files (PDF): Anatase TiO<sub>2</sub> (PDF 21-1272), Rutile TiO<sub>2</sub> (PDF 04-004-4338), Ti<sub>10</sub>O<sub>19</sub> (PDF 00-011-0474), Ti<sub>9</sub>O<sub>17</sub> (PDF 00-050-0791), Ti<sub>8</sub>O<sub>15</sub> (PDF 00-050-0790), Ti<sub>7</sub>O<sub>13</sub> (PDF 00-050-0789), Ti<sub>6</sub>O<sub>11</sub> (PDF 00-050-0788) and Ti<sub>5</sub>O<sub>9</sub> (PDF 00-051-0641).

To assess the impact of activated charcoal on the reduction process, two TiO<sub>2</sub> samples were treated under identical reaction conditions (9 h and 12 h annealing at 1100 °C) within the tube furnace, but without activated charcoal. The resulting XRD spectra only indicated the presence of rutile Ti<sub>0.936</sub>O<sub>2</sub> (PDF 89-0554), signifying the absence of notable reduction or oxygen deficiency (Figure S3). This observation highlights the vital role of activated charcoal in driving the reduction reaction.

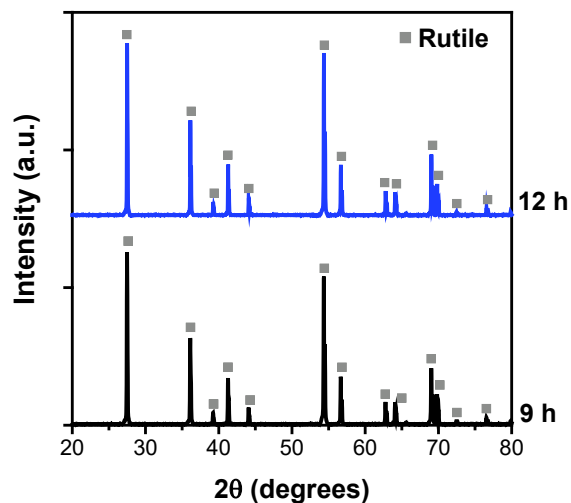


**Figure S3:** XRD patterns of anatase TiO<sub>2</sub> subjected to similar thermal annealing at 1100 °C for 9 h and 12 h (as marked) but without the presence of charcoal.

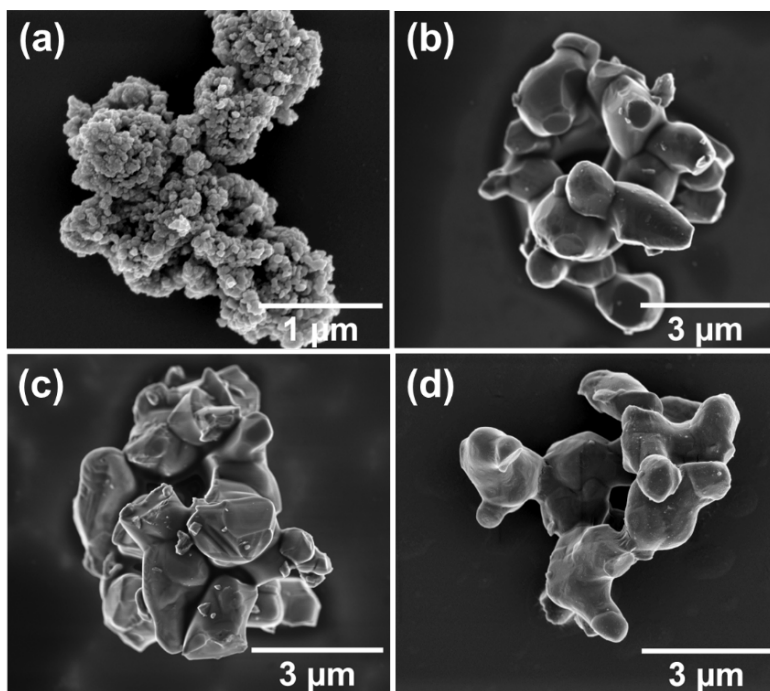


**Figure S4:** SEM images of (a) anatase TiO<sub>2</sub> and TiO<sub>2-x</sub> carbothermally reduced for (b) 2 h, (c) 6 h and (d) 9 h.

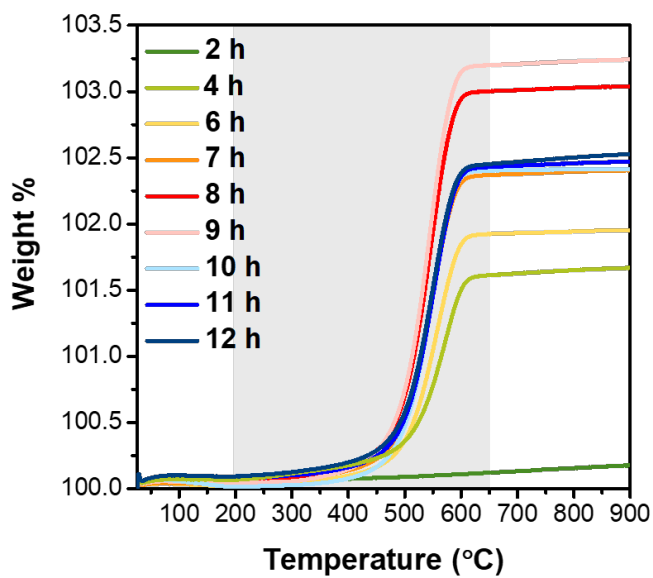
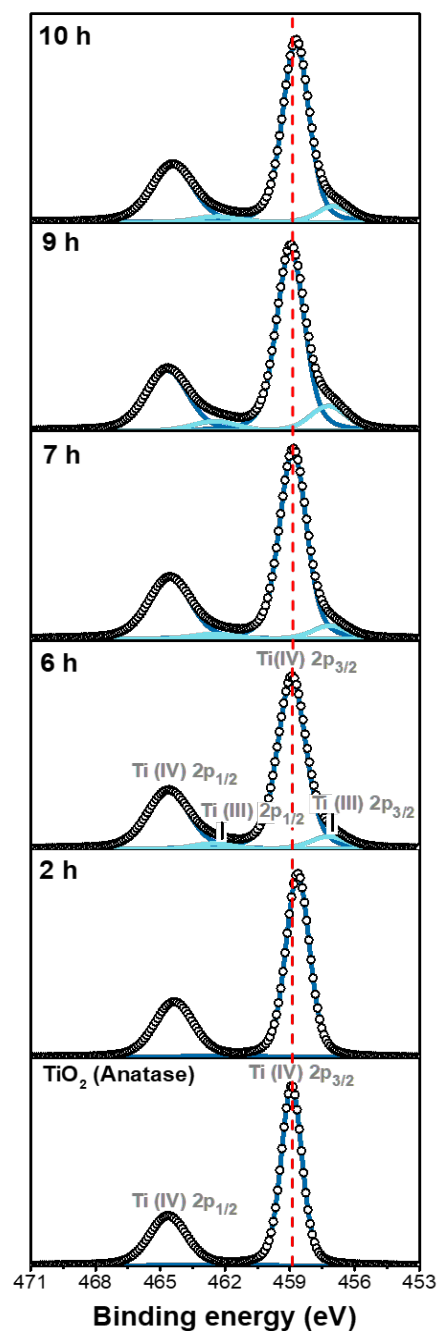


**Figure S5:** TGA analyses, heating from 25 to 900 °C at 10 °Cmin<sup>-1</sup> under O<sub>2</sub> flow, of the TiO<sub>2-x</sub> samples prepared by carbothermally reducing TiO<sub>2</sub> for 2-12 h.

**Table S1:** Calculated oxygen deficiency ( $x$ ) and respective formulae for  $\text{TiO}_{2-x}$ .

<b>Duration at 1100 °C (h)</b>	<b>Oxygen deficiency (<math>x</math>)</b>	<b>Formula for <math>\text{TiO}_{2-x}</math></b>
2	0.003	$\text{TiO}_{1.997}$
4	0.076	$\text{TiO}_{1.924}$
6	0.101	$\text{TiO}_{1.899}$
7	0.114	$\text{TiO}_{1.886}$
8	0.144	$\text{TiO}_{1.856}$
9	0.153	$\text{TiO}_{1.847}$
10	0.117	$\text{TiO}_{1.883}$
11	0.115	$\text{TiO}_{1.885}$
12	0.115	$\text{TiO}_{1.885}$



The two peaks present in the Ti 2p spectrum of anatase TiO<sub>2</sub> at 458.9 and 464.6 eV were attributed to Ti (IV) 2p<sub>3/2</sub> and Ti (IV) 2p<sub>1/2</sub> chemical environments, respectively. Defective rutile TiO<sub>2</sub> obtained after 2 h of reduction showed the same two peaks but positioned at 458.6 and 464.4 eV, in accordance with rutile Ti (IV) oxide [1]. Ti (III) 2p<sub>3/2</sub> and Ti (III) 2p<sub>1/2</sub> peaks emerged by 4 h (not shown), and these two peaks, along with Ti (IV) 2p<sub>3/2</sub> and Ti (IV) 2p<sub>1/2</sub> peaks shifted towards higher BE with increasing reduction time up to 9 h. However, along with the change in phase composition by 10 h, all peaks shifted to negative BE with Ti (IV) 2p<sub>3/2</sub> and Ti (IV) 2p<sub>1/2</sub> at 458.7 and 464.5 eV and Ti (III) 2p<sub>3/2</sub> and Ti (III) 2p<sub>1/2</sub> at 457.0 and 462.3 eV, respectively.

**Figure S6:** High resolution XPS scans of Ti 2p for TiO<sub>2</sub> (anatase) and carbothermally reduced TiO<sub>2-x</sub> synthesised at 2, 6, 7, 9 and 10 h (as marked).

EPR spin Hamiltonian simulations were performed using the easyspin package. Three parameters need to be included in these fitting, the g-values: g-parallel and g-perpendicular, and a Lorentzian linewidth. To first order, g-parallel and g-perpendicular are equal to:

$$g_{\parallel} = g_e \left(1 - \frac{4\zeta}{\Delta_1}\right) \quad (\text{S1})$$

$$g_{\perp} = g_e \left(1 - \frac{2\zeta}{\Delta_2}\right) \quad (\text{S2})$$

Where  $g_e$  is the free electron g-value, zeta the spin-orbit coupling and  $\Delta_1$  and  $\Delta_2$  the d-orbital energy level splittings (see Figure S7 inset). This allows the relative energy levels of the d-manifold of the  $\text{Ti}^{3+}$  ion to be estimated. The g parallel value did not significantly change across all samples. Interestingly though, the g perpendicular value followed the same trend seen for the intensity of the  $\text{Ti}^{3+}$  signal, increasing from 1.972 to 1.976 upon annealing 8-9 h. It then decreased back to 1.972 upon further annealing. A larger g perpendicular value would correspond to an increase in  $\Delta_2$  energy spacing, and thus likely reflects a larger ligand distortion of the catalytically active  $\text{Ti}^{3+}$  fraction. The g parallel value did not change significantly across all samples. The linewidth tended to increase with annealing time.

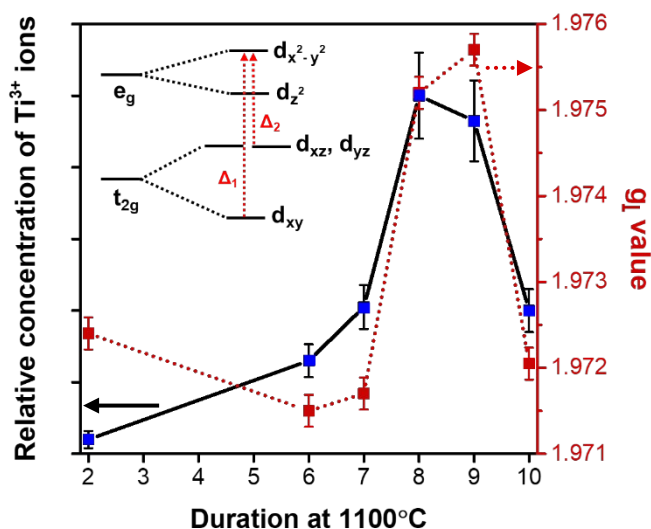


**Figure S7:** Relative concentration of  $\text{Ti}^{3+}$  ions as a function of annealing time. The concentration was calculated by taking double integration of the raw EPR data. A linear baseline was used. The percentage error is estimated to be 10% of the signal. Change in the g perpendicular value as a function of annealing time, as estimated from spin Hamiltonian simulations. The uncertainty in these measurements is in the fourth decimal place ( $\pm 0.0005$ ). The inset shows the energy levels of the d-manifold of rutile, with the energy spacing relevant to determining the g-tensor values marked [2-4].

The positions of the valence band maxima (VBM) and conduction band minima (CBM) of these materials were determined with the use of the  $E_g$  band edge from high-resolution VB spectrum obtained from XPS characterisation ( $CBM = VBM - E_g$ ) (Figure S8).

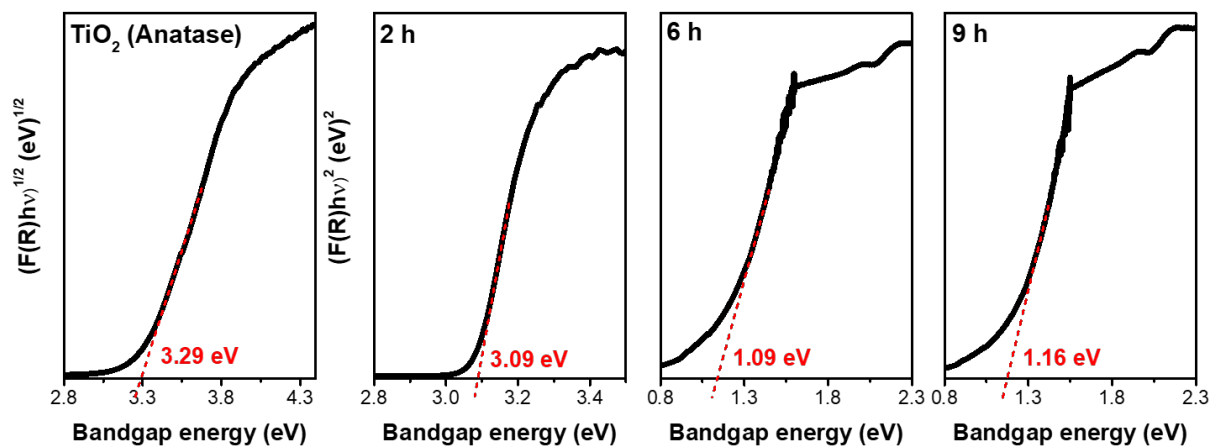


**Figure S8:** Kubelka-Munk plots derived from DRS for anatase  $TiO_2$  and  $TiO_{2-x}$  reduced for 2, 6 and 9 h (as marked).

The calculated band positions were plotted against hydroxyl and superoxide radical forming redox potentials and are shown in Figure S9. These data suggest that mild reduction, hence less defects in the  $TiO_2$  lattice, caused negative shifting of the CBM, with higher superoxide radical ( $O_2^{\cdot-}$ ) forming ability compared to anatase  $TiO_2$ . However, complete Magnéli phase formation by 6 h accompanied by formation of bulk defects caused significant bandgap reduction with substantial positive shifts in both CBM and VBM.

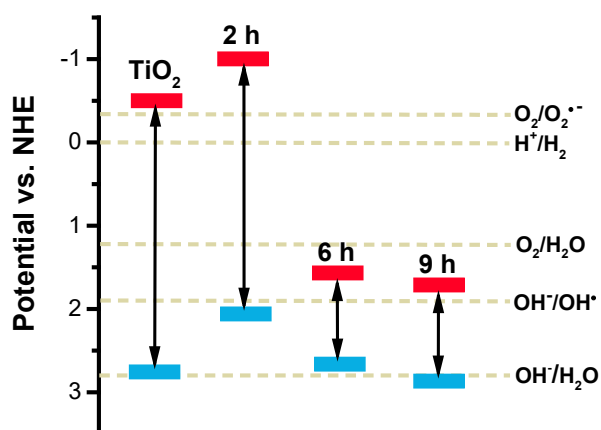


**Figure S9:** Band positions of the samples with respect to hydroxyl and superoxide radical forming potentials at  $pH=0$ .

Lifetimes of photogenerated charges of the formed TiO<sub>2-x</sub> were determined via photoluminescence (PL) spectroscopy. All decay curves were fitted into a biexponential function using Equation S3 [5];

$$I(t) = A_1 \exp(-t/\tau_1) + A_2 \exp(-t/\tau_2) \quad (\text{S3})$$

Where I(t) represents the PL intensity at time t, A<sub>1</sub> and A<sub>2</sub> are the pre-exponential factors and τ<sub>1</sub> and τ<sub>2</sub> are the shorter and longer lifetime components, respectively. The average lifetimes (τ<sub>avg</sub>) of all TiO<sub>2-x</sub> (Table S2) were determined as follows [6]:

$$\tau_{avg} = \frac{A_1\tau_1^2 + A_2\tau_2^2}{A_1\tau_1 + A_2\tau_2} \quad (\text{S4})$$

**Table S2:** Calculated lifetimes and their contribution to the effective lifetime of photogenerated charge carriers in carbothermally reduced TiO<sub>2-x</sub>.

Annealing time (h)	τ <sub>1</sub> (ns)	Contribution (%)	τ <sub>2</sub> (ns)	Contribution (%)	τ <sub>avg</sub> (ns)
0 (TiO <sub>2</sub> )	2.43	99.1	0.56	0.9	2.42
2	0.46	94.2	2.66	5.8	1.03
6	0.35	98.2	6.52	1.8	1.93
7	0.36	98.5	6.39	1.5	1.68
8	0.34	98.5	6.54	1.5	1.76
9	0.38	97.0	6.86	3.0	2.69
10	0.34	96.1	6.27	3.9	2.90
11	0.34	97.2	6.26	2.8	2.40
12	0.34	97.4	6.36	2.6	2.34

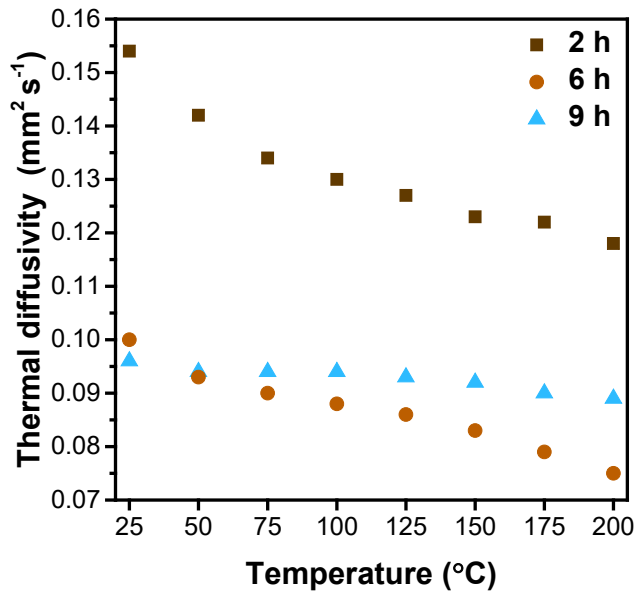


**Figure S10:** Thermal diffusivity of  $\text{TiO}_{2-x}$  carbothermally reduced for 2, 6 and 9 h.

**Table S3:** Summary of Magnéli phase synthesis strategies and products obtained.

Ti precursor	Synthesis/Treatment of the precursor	Reduction conditions	Product composition	Ref.
Anatase TiO <sub>2</sub> nanoparticles	Anatase TiO <sub>2</sub> mixed with carbon black and ball milled for 24 h at 200 rpm followed by oven drying at 80 °C.	Heated in a tube furnace at 1100 °C for 3 h under Ar flow with a flow rate of 300 mL/min.	Anatase/Rutile/Ti <sub>9</sub> O <sub>17</sub>	[7]
Rutile TiO <sub>2</sub>	-	Reduced at 800 °C (at a heating rate of 10°C/min) under pure H <sub>2</sub> gas at 1.0 L/min	A mixture of rutile TiO <sub>2</sub> and Ti <sub>9</sub> O <sub>17</sub> .	[8]
Anatase TiO <sub>2</sub>	TiO <sub>2</sub> mixed with synthetic graphite, distilled water and carboxymethyl cellulose and oven dried at 120 °C. The mixture was pelletized by uniaxial hydraulic press.	Reduction was conducted at 1000°C under Ar atmosphere (1.00 NL/min) in a fixed bed reactor in a vertical tube furnace for 5 h.	TiO <sub>2</sub> / Ti <sub>9</sub> O <sub>17</sub> /Ti <sub>8</sub> O <sub>15</sub>	[9]
Anatase TiO <sub>2</sub>	-	Crucible containing anatase TiO <sub>2</sub> is placed between two crucibles containing activated charcoal. Heated at 1100 °C (with a heating rate of 5 °C/min) under Ar atmosphere (0.5 NL/h) for 6 h.	Ti <sub>9</sub> O <sub>17</sub> (~90 wt%) and possibly Ti <sub>10</sub> O <sub>19</sub>	<b>This work</b>
Anatase TiO <sub>2</sub>	TiO <sub>2</sub> was pelletized via uniaxial pressing and then the pellets were sintered at 1327 °C for 5 h in air.	7% H <sub>2</sub> (Ar) atmosphere for 3.5 h at 1147 °C	A mixture of Ti <sub>9</sub> O <sub>17</sub> and Ti <sub>8</sub> O <sub>15</sub> .	[10]
Anatase TiO <sub>2</sub>	TiO <sub>2</sub> was mixed with carbon black (4.00 wt% carbon content) and ball milled.	Heated in vacuum furnace from 1000 °C for 2 h.	Ti <sub>9</sub> O <sub>17</sub> /Ti <sub>7</sub> O <sub>13</sub> /Ti <sub>6</sub> O <sub>11</sub>	[11]
TiO <sub>2</sub> (Degussa, P25)	P25 was oxidised (800 °C/2 h) to remove any organic contaminants.	Reduced at 1000 °C (at a heating rate of 1 °C/min) for 2 h in a 4% H <sub>2</sub> (Ar) atmosphere	A mixture of Ti <sub>9</sub> O <sub>17</sub> /Ti <sub>6</sub> O <sub>11</sub> .	[12]
Amorphous TiO <sub>x</sub>	Addition of H <sub>2</sub> O <sub>2</sub> to a mixture of TiCl <sub>4</sub> and ethylenediamine - tetraacetic acid to form colloidal TiO <sub>x</sub> followed by precipitating and filtering the resulting mixture to get amorphous TiO <sub>x</sub> .	Heated in a quartz tubular reactor at 1050 °C (with a heating rate of 5 °C/min) for 2 h under 10% H <sub>2</sub> (Ar) stream fed at 20 cc/min.	A mixture of Ti <sub>9</sub> O <sub>17</sub> /Ti <sub>6</sub> O <sub>11</sub> .	[13]
Anatase TiO <sub>2</sub>	-	Crucible containing anatase TiO <sub>2</sub> is placed between two crucibles containing activated charcoal. Heated at 1100 °C (with a heating rate of 5 °C/min) under Ar atmosphere (0.5 NL/h) for 7-8 h.	Mixtures of Ti <sub>9</sub> O <sub>17</sub> , Ti <sub>8</sub> O <sub>15</sub> , Ti <sub>7</sub> O <sub>15</sub> and Ti <sub>6</sub> O <sub>11</sub>	<b>This work</b>
Titanium isopropoxide (TTIP)	TTIP solution is converted to Ti(OH) <sub>2</sub> in water which is then converted to titanium nitrate using HNO <sub>3</sub> . A colloidal crystal template formed of silica nanoparticles was added into the above solution followed by	Heated under H <sub>2</sub> flow with a flow rate of 200 mL/min in a tube furnace at 800 °C for 5 h.	Mesoporous Ti <sub>6</sub> O <sub>11</sub> with trace amounts of anatase TiO <sub>2</sub>	[14]

	drying at 120 °C and further at 200 °C for 3 h.			
Anatase TiO <sub>2</sub>	Anatase TiO <sub>2</sub> was formed by hydrothermally treating Ti(OH) <sub>2</sub> at 200-300 °C for 3 h.	Reduced in a Tamman furnace under H <sub>2</sub> atmosphere (flow rate of 5 L/min) at 1000 °C for 5.5 h.	Mixture of Ti <sub>9</sub> O <sub>17</sub> , Ti <sub>8</sub> O <sub>15</sub> and Ti <sub>5</sub> O <sub>9</sub> .	[15]
TiO <sub>2</sub> powder	Thermoplastic extrusion was used to form TiO <sub>2</sub> fibres. For this process, stearic acid and polyethylene were used as the pre-coating material and binder, respectively.	TiO <sub>2</sub> fibres embedded in carbon black powder were reduced at 1200 °C and 1300 °C from 1-24 h in an Ar atmosphere.	Mixture of Ti <sub>10</sub> O <sub>19</sub> , Ti <sub>9</sub> O <sub>17</sub> , Ti <sub>8</sub> O <sub>15</sub> , Ti <sub>6</sub> O <sub>11</sub> , Ti <sub>5</sub> O <sub>9</sub> , Ti <sub>4</sub> O <sub>7</sub> , Ti <sub>3</sub> O <sub>5</sub> and TiO <sub>2</sub> .	[16]
Anatase TiO <sub>2</sub>	-	Crucible containing anatase TiO <sub>2</sub> is placed between two crucibles containing activated charcoal. Heated at 1100 °C (with a heating rate of 5 °C/min) under Ar atmosphere (0.5 NL/h) for 9 h.	Ti <sub>6</sub> O <sub>11</sub> is obtained as the major phase (≥60 wt%), with Ti <sub>5</sub> O <sub>9</sub> , Ti <sub>7</sub> O <sub>13</sub> , Ti <sub>8</sub> O <sub>15</sub> and Ti <sub>9</sub> O <sub>17</sub> .	<b>This work</b>

### Characterisation of GO aerogels

The density of the aerogel ( $d$ ) was determined using Equation S5 [17].

$$d = \frac{m}{\pi r^2 h} \quad (\text{S5})$$

where  $m$  (g) is the average mass (0.325 g),  $r$  is the radius (in cm, 2.25 cm) and  $h$  is the thickness (in cm, 0.2 cm) of the aerogel used in the solar steam generation experiments.

The optimised GO aerogel (Figure S11) had a calculated density of 0.102 g cm<sup>-3</sup>, guaranteeing its self-floating ability. This aerogel was a 2D circular sponge-like membrane with 45 mm diameter and 2 mm thickness. Additionally, at room temperature (21 °C), the GO aerogel displayed a low thermal conductivity of 0.015 W m<sup>-1</sup> K<sup>-1</sup> in agreement with the literature [18], to facilitate optimal heat localisation for efficient heat generation.

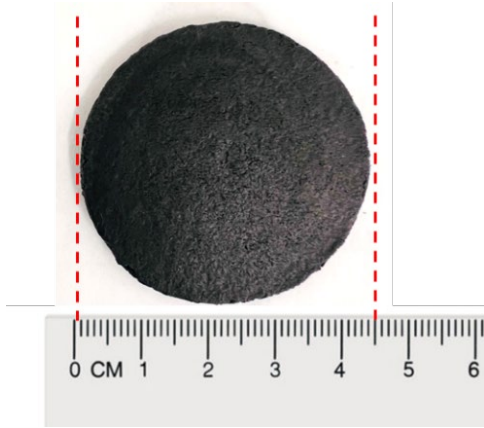


**Figure S11:** Top view of the as prepared GO aerogel.

SEM characterisation (Figure S12) revealed a highly porous structure consisting of a 3D interconnected network of GO. Hence, the prepared GO aerogel possesses a combination of qualities, including its porous nature, low density and favourable thermal conductivity, positioning it as an excellent substrate material for solar steam generation.

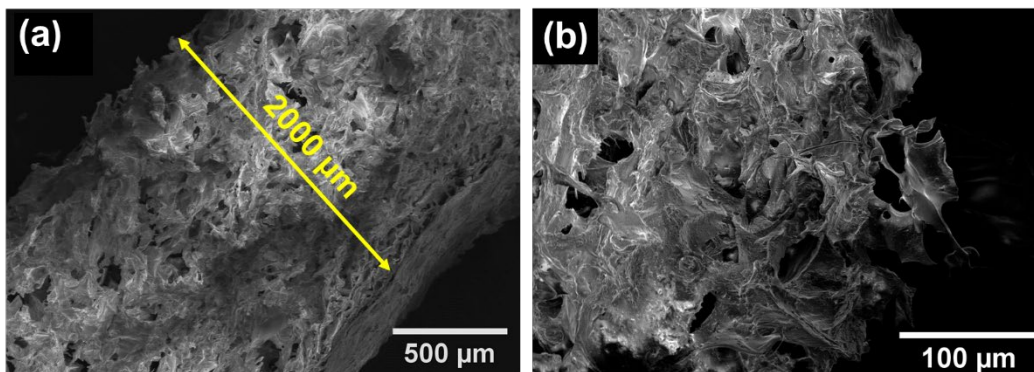


**Figure S12:** (a) Cross section of the aerogel showing the thickness is 0.2 cm and (b) porous nature of the GO network.

#### Calculating solar water evaporation rate and energy conversion efficiency

The evaporation rate of interfacial water ( $v$ ) can be related to the mass of water evaporated ( $\Delta m$  (kg)), surface area of the aerogel ( $s$  ( $m^2$ )) and the evaporation time ( $\Delta t$  (h)) as follows [17]:

$$v = \frac{\Delta m}{s \times \Delta t} \quad (S6)$$

The efficiency of solar-to-vapour conversion can be expressed as given in Equation S7:

$$\eta = \frac{v \times H_{LV}}{P_{in}} \quad (S7)$$

where  $v$  ( $\text{kg m}^{-2}\text{h}^{-1}$ ) denotes the rate of water evaporation under solar light.  $P_{\text{in}}$  ( $\text{kW m}^{-2}$ ) is the light power or the energy of the incident light.  $H_{\text{LV}}$  ( $\text{J kg}^{-1}$ ) is the latent enthalpy of liquid-vapour phase change and can be determined by Equation S8 [19, 20]:

$$H_{\text{LV}(T)} = 1.91846 \times 10^6 \left[ \frac{T_1}{T_1 - 33.91} \right]^2 \quad (\text{S8})$$

where  $T_1$  (K) is the stable average temperature on the surface of the solar evaporator [17].

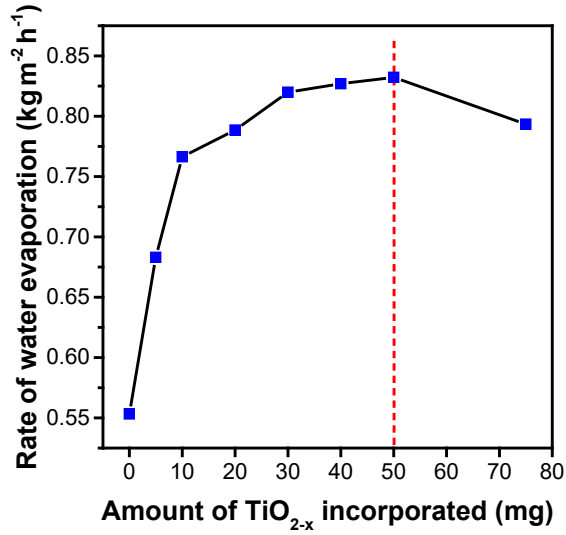


**Figure S13:** Rate of water evaporation for GO- $\text{TiO}_{2-x}$  aerogels with different loadings of 9 h  $\text{TiO}_{2-x}$ .

## References

1. Biesinger, M.C., et al., *Resolving surface chemical states in XPS analysis of first row transition metals, oxides and hydroxides: Sc, Ti, V, Cu and Zn*. Appl. Surf. Sci., 2010. **257**(3): p. 887-898.
2. Zhou, Y., et al., *Enhanced photoreduction of Cr(VI) and photooxidation of NO over TiO<sub>2-x</sub> mesoporous single crystals*. RSC Adv., 2017. **7**(88): p. 55927-55934.
3. Chiesa, M., et al., *Charge trapping in TiO<sub>2</sub> polymorphs as seen by Electron Paramagnetic Resonance spectroscopy*. Physical Chemistry Chemical Physics, 2013. **15**(24): p. 9435.
4. Wen, B., et al., *Electronic structure and photoabsorption of Ti<sup>3+</sup> ions in reduced anatase and rutile TiO<sub>2</sub>*. Physical Chemistry Chemical Physics, 2018. **20**(26): p. 17658-17665.
5. Wen, X., et al., *Ultrafast electron transfer in the nanocomposite of the graphene oxide–Au nanocluster with graphene oxide as a donor*. J. Mater. Chem. C, 2014. **2**(19): p. 3826-3834.
6. Wang, Q., et al., *Silk fibroin-derived nitrogen-doped carbon quantum dots anchored on TiO<sub>2</sub> nanotube arrays for heterogeneous photocatalytic degradation and water splitting*. Nano Energy, 2020. **78**: p. 105313.
7. Wang, F., et al., *Formation mechanisms of interfaces between different Ti<sub>n</sub>O<sub>2n-1</sub> phases prepared by carbothermal reduction reaction*. CrystEngComm, 2019. **21**(3): p. 524-534.
8. Liu, J., et al., *Pressure Dependence of Electrical Conductivity of Black Titania Hydrogenated at Different Temperatures*. J. Phys. Chem. C, 2019. **123**(7): p. 4094-4102.
9. Dewan, M.A.R., G. Zhang, and O. Ostrovski, *Carbothermal Reduction of Titania in Different Gas Atmospheres*. Metall. Mater. Trans. B, 2009. **40**(1): p. 62-69.
10. Radecka, M., et al., *Effect of oxygen nonstoichiometry on photo-electrochemical properties of TiO<sub>2-x</sub>*. Journal of Power Sources, 2007. **173**(2): p. 816-821.
11. Zhu, R., et al., *Magnéli phase Ti<sub>4</sub>O<sub>7</sub> powder from carbothermal reduction method: formation, conductivity and optical properties*. J. Mater. Sci.: Mater. Electron., 2013. **24**(12): p. 4853-4856.
12. Martyanov, I.N., et al., *Enhancement of TiO<sub>2</sub> visible light photoactivity through accumulation of defects during reduction–oxidation treatment*. J. Photochem. Photobiol., A, 2010. **212**(2): p. 135-141.
13. Siracusano, S., et al., *Preparation and characterization of titanium suboxides as conductive supports of IrO<sub>2</sub> electrocatalysts for application in SPE electrolyzers*. Electrochim. Acta, 2009. **54**(26): p. 6292-6299.
14. Kuroda, Y., et al., *Templated Synthesis of Carbon-Free Mesoporous Magnéli-Phase Titanium Suboxide*. Electrocatalysis, 2019. **10**(5): p. 459-465.
15. Vasilevskaia, A.K., et al., *Formation of nonstoichiometric titanium oxides nanoparticles Ti<sub>n</sub>O<sub>2n-1</sub> upon heat-treatments of titanium hydroxide and anatase nanoparticles in a hydrogen flow*. Russ. J. Appl. Chem., 2016. **89**(8): p. 1211-1220.
16. Adamaki, V., et al., *Manufacturing and characterization of Magnéli phase conductive fibres*. J. Mater. Chem. A, 2014. **2**(22): p. 8328-8333.
17. Li, W., et al., *Highly efficient solar vapour generation via self-floating three-dimensional Ti<sub>2</sub>O<sub>3</sub>-based aerogels*. Colloids Surf., A, 2022. **634**: p. 128031.
18. Hu, X., et al., *Tailoring Graphene Oxide-Based Aerogels for Efficient Solar Steam Generation under One Sun*. Adv. Mater., 2017. **29**(5): p. 1604031.
19. Zhou, L., et al., *3D self-assembly of aluminium nanoparticles for plasmon-enhanced solar desalination*. Nat. Photonics, 2016. **10**(6): p. 393-398.
20. Li, X., et al., *Measuring Conversion Efficiency of Solar Vapor Generation*. Joule, 2019. **3**(8): p. 1798-1803.